Chatter Stability Characterization of Full-Immersion End-Milling Using a Generalized Modified Map of the Full-Discretization Method, Part 1: Validation of Results and Study of Stability Lobes by Numerical Simulation

Chigbogu G. Ozoegwu, Sam N. Omenyi

Abstract—The objective in this work is to generate and discuss the stability results of fully-immersed end-milling process with parameters; tool mass $m = 0.0431$kg, tool natural frequency $\omega_n = 5700$ rads^{-1}, damping factor $\xi = 0.02$ and workpiece cutting coefficient $C = 3.5 \times 10^7$Nm$^{-7/4}$. Different no of teeth is considered for the end-milling. Both 1-DOF and 2-DOF chatter models of the system are generated on the basis of non-linear force law. Chatter stability analysis is carried out using a modified form (generalized for both 1-DOF and 2-DOF models) of recently developed method called Full-discretization. The full-immersion three tooth end-milling together with higher toothed end-milling processes has secondary Hopf bifurcation lobes (SHBL's) that exhibit one turning (minimum) point each. Each of such SHBL is demarcated by its minimum point into two portions; (i) the Lower Spindle Speed Portion (LSSP) in which bifurcations occur in the right half portion of the unit circle centred at the origin of the complex plane and (ii) the Higher Spindle Speed Portion (HSSP) in which bifurcations occur in the left half portion of the unit circle. Comments are made regarding why bifurcation lobes should generally get bigger and more visible with increase in spindle speed and why flip bifurcation lobes (FBL's) could be invisible in the low-speed stability chart but visible in the high-speed stability chart of the fully-immersed three-tooth miller.

Keywords—Chatter, flip bifurcation, modified full-discretization map stability lobe, secondary Hopf bifurcation.

I. INTRODUCTION

COMPONENTS of high dimensional integrity are in ever increasing need. Machine tools such as Lathe and Milling machines are needed for production of such components. Machine tools would not perform effectively under highly disturbed situations thus the need for vibration control in such machines. Achieving good surface finish and high productivity are two opposed demands in machining operation. This means that ascertaining safe operation range for good product, improved tool life and design of machine tools is necessary.

C. G. Ozoegwu is with the Department of Mechanical Engineering, Nnamdi Azikiwe University, Awka, PMB 5025, Nigeria (phone: +2348080241618; e-mail: chigbogug@yahoo.com).
S. N. Omenyi is with the Department of Mechanical Engineering, Nnamdi Azikiwe University, Awka, PMB 5025, Nigeria (e-mail: sam.omenyi@unizik.edu.ng).

A typical machining process of major importance is the end-milling in which a machined surface that is at right angle with the cutter axis results as shown Fig. 1. In end-milling, cutters equipped with shanks for mounting on the spindle are utilized.
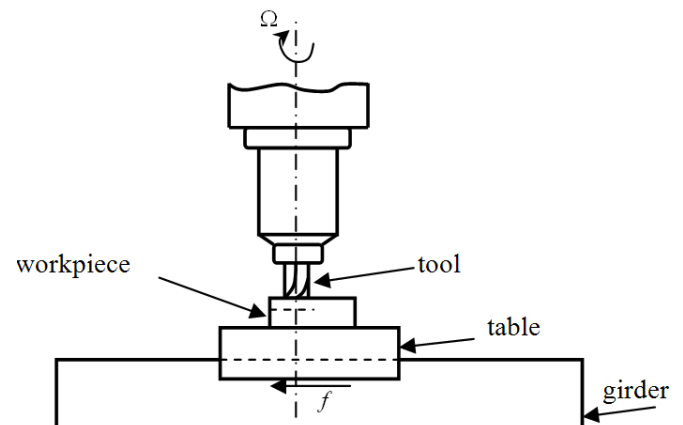

Fig. 1 End-milling

Unstable regenerative machine tool vibration is basically called chatter. Chatter invariably results whenever there is dynamic interaction between the tool and the workpiece of a milling process under unstable cutting parameter combination. Forced, self-exited and damped natural vibrations combine to compound the dynamics of milling process. The forced vibration component is driven by a periodic force stemming from regular engagement and disengagement of tool and workpiece. Regenerative effect is underpinned as the major cause of the self-exited vibrations (mechanical chatter) in machining [1]. Arnold first suggested regenerative effects as the potential cause of chatter and is now arguably considered the cause of the most detrimental type of machine tool vibration [2]. Chatter occurring during machining operation thus results from cutting force variation caused by disturbance-induced surface waviness of regenerative effects.

Effects of periodic chip thickness and delayed position on the present position of the tool result in periodic delay differential equation (DDE) models for regenerative vibrations of milling. Among the various advanced methods utilized in

World Academy of Science, Engineering and Technology
International Journal of Mechanical and Mechatronics Engineering
Vol:7, No:3, 2013

tracking the approximate stability transition curve of regenerative milling are; the finite element in time [3], [4], Chebyshev Polynomials [4], [5], semi-discretization [6], Fargue-type approximation [7], [8]. The normal procedure is to generate a finite dimensional discrete approximation to the governing infinite dimensional periodic DDE and carrying out eigen-value analysis of resulting finite monodromy operator as cutting parameters vary.

The semi-discretization concept as utilized in a recently developed method called Full-discretization [9] is utilized here in deriving an alternate finite map called modified full-discretization map. The modified full-discretization map is generalized for both 1-DOF and 2-DOF end-milling. The system considered is a Perspex or wood end milling CNC machine considered in [8] to have the following modal parameters; mass $m = 0.0431$kg, Natural frequency $\omega_n = 5700\,\text{rads}^{-1}$, and damping factor $\xi = 0.02$. The stability characterization of the system is in the form of stability charts in which parameter space of spindle speed and dept of cut are demarcated into stable and unstable domains by stability transition curves. In literature such charts are normally validated by comparing results of two different methods [3], [4] but in this work accurate MATLAB dde23 solution of several parameter points are used in validation of both cases of 1-DOF and 2-DOF end-milling. Stability or instability of MATLAB dde23 solutions are seen to be independent of history of end-milling chatter model. This is a unique feature of this work.

Parameter points are picked from the stability transition curves and substituted into the monodromy operator for extraction of critical characteristic multipliers. It results that in conformity with literature [10], either a pair of complex conjugate critical characteristic multipliers or a critical characteristic multiplier of -1 exists on the stability transition curves of end-milling. The three tooth fully-immersed 1-DOF end-milling together with higher toothed fully-immersed 1-DOF end-milling has secondary Hopf bifurcation lobes (SHBL's) that exhibit one minimum point each. Each of such SHBL is demarcated by its minimum point into Lower Spindle Speed Portion (LSSP) in which bifurcations occur in the right half portion of the unit circle centered at the origin of the complex plane and Higher Spindle Speed Portion (HSSP) in which bifurcations occur in the left half portion of the unit circle. The real part of the pair of critical characteristic multipliers varies from about 1 to about 0 as a critical point moves from start to end of a LSSP. When the critical point moves from start to end of a HSSP the real part of the pair of critical characteristic multipliers varies from about 0 to about -1. This means that bifurcation gets towards flip towards the end of a SHBL. Comments are made regarding why bifurcation lobes should generally get bigger and more visible with increase in spindle speed. It is concluded in this work that even when flip bifurcation is not seen, it is expected to occur in the immediate vicinity of intersection of two SHBL's. These form part of novelty of contribution of this work.

II. MATHEMATICAL MODEL

A. Single Degree of Freedom Model

The dynamical model shown in Fig. 2 is a 1-DOF vibration model of an end-milling tool in which the tool is given a spindle speed Ω in revolutions per minute (rpm) while the workpiece has a prescribed feed velocity v imparted on it via the worktable. The tool and workpiece are engaged at a radial immersion of $\rho = B/D$ (ratio of radial depth of cut to tool diameter). The parameters of the milling process as depicted on the dynamical model are; m mass of tool, c the equivalent viscous damping coefficient modeling the hysteretic damping of the tool and k the stiffness of the tool.
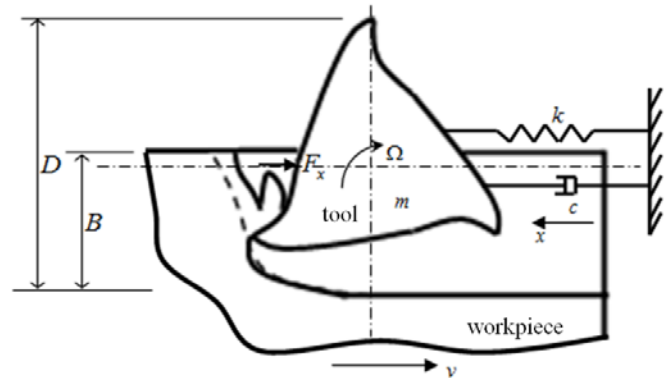

Fig. 2 Dynamical model of 1-DOF end-milling

The free-body diagram for the tool dynamics when the motion of the tool $x(t)$ is considered to be a summation of feed motion and vibrations is as shown in Fig. 3.
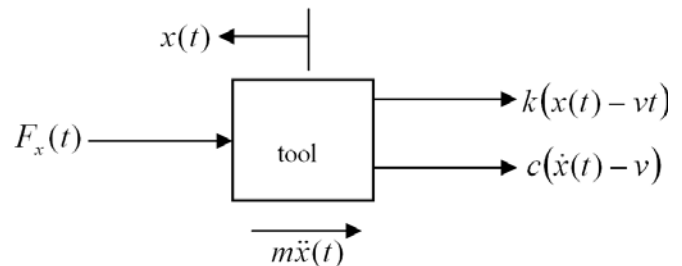

Fig. 3 Free-body diagram of tool dynamics

The differential equation governing the motion of the tool as seen from the free-body diagram becomes

$$m\ddot{x}(t) + c[\dot{x}(t) - v] + k[x(t) - vt] + F_x(t) = 0 \qquad (1)$$

A tool-workpiece disposition as shown in Fig. 4 is considered for the jth tooth of the tool. In Fig. 4 the cutting force is considered as having normal and tangential components designated $F_{\text{norm},j}(t)$ and $F_{\text{tan},j}(t)$ respectively. Axial component of cutting force is neglected because helix angle is considered zero. The $x-$component of cutting force for the tool thus becomes

World Academy of Science, Engineering and Technology
International Journal of Mechanical and Mechatronics Engineering
Vol:7, No:3, 2013

$$F_x(t) = \sum_{j=1}^{N} g_j(t)\left[F_{\text{norm},j}(t)\sin\theta_j(t) + F_{\text{tan},j}(t)\cos\theta_j(t)\right] \quad (2)$$

N is the number teeth on the milling tool indexed with the values $j = 1, 2, 3......N$. The instantaneous angular position of jth tooth $\theta_j(t)$ is measured clockwise relative to the negative y−axis to give

$$\theta_j(t) = \left(\frac{\pi\Omega}{30}\right)t + (j-1)\frac{2\pi}{N} + \alpha \quad (3)$$

where α is the initial angular position of the tooth indexed 1. Screen or switching function $g_j(t)$ for the jth tooth either have the values 1 or 0 depending on whether the tooth is active or not. At full-radial immersion $\rho = 1$, the screen function is formulated to have the form

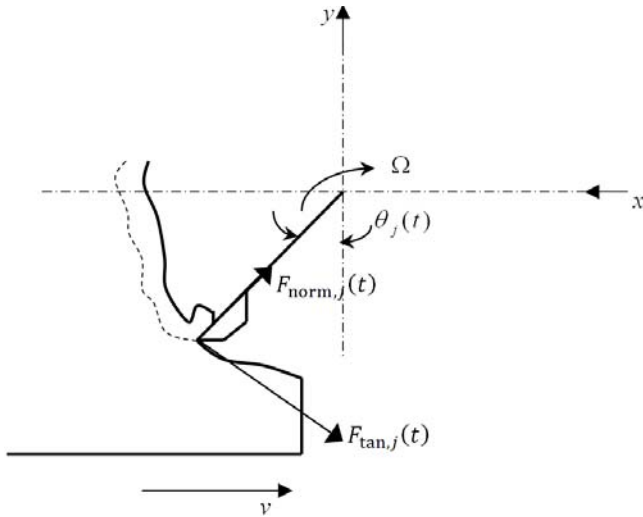$$g_j(t) = \frac{1}{2}\{1 + \text{sgn}[\sin\theta_j(t)]\}. \quad (4)$$

Fig. 4 Milling tooth-workpiece disposition

The cutting forces on jth tooth are given by the non-linear law

$$F_{\text{tan},j}(t) = C_{tan}w\left[f_a\sin\theta_j(t)\right]^\gamma \quad (5a)$$

$$F_{\text{norm},j}(t) = C_{norm}w\left[f_a\sin\theta_j(t)\right]^\gamma = \mathcal{X}F_{\text{tan},j}(t) \quad (5b)$$

where w is depth of cut, C_{tan} and C_{norm} are the tangential and normal cutting coefficients associated with the workpiece, $\mathcal{X}$ is the ratio C_{norm}/C_{tan}, f_a is the actual feed given as $x(t) - x(t-\tau)$ which is the difference between present and one period delayed position of tool and γ is an exponent that is usually less than one having a value of $3/4$ for the three-quarter rule utilized here. Works of Balint, Bali and Tlusty are reported in [10] to popularize the value of 0.3 for $\mathcal{X}$. Equations (2) and (5) taken together give

$$F_x(t) = wq(t)[x(t) - x(t-\tau)]^\gamma \quad (6)$$

where $q(t) = \sum_{j=1}^{N} g_j(t)C\sin^\gamma\theta_j(t)\left[\mathcal{X}\sin\theta_j(t) + \cos\theta_j(t)\right]$ is a $\tau(= 60/N\Omega)$ periodic function. The vibration of the tool has two components namely; the τ-periodic response $x_t(t)$ due to periodic force of tool/workpiece interaction and the regenerative perturbations $z(t)$. Then

$$x(t) = vt + x_t(t) + z(t). \quad (7)$$

Substitution of (6) and (7) into (1) gives

$$m\ddot{x}_t(t) + c\dot{x}_t(t) + kx_t(t) + m\ddot{z}(t) + c\dot{z}(t) + kz(t) = -wq(t)\{vt + [z(t) - z(t-\tau)]\}^\gamma \quad (8)$$

Without perturbation, (8) simplifies to

$$m\ddot{x}_t(t) + c\dot{x}_t(t) + kx_t(t) = -wq(t)(v\tau)^\gamma \quad (9)$$

Equation (9) governs the periodic motion of the system driven by a periodic force $F_p(t) = -wq(t)(v\tau)^\gamma$. Equation (9) means that (8) becomes

$$m\ddot{z}(t) + c\dot{z}(t) + kz(t) = wq(t)(v\tau)^\gamma - wq(t)\{v\tau + [z(t) - z(t-\tau)]\}^\gamma \quad (10)$$

Put in Taylor series about $v\tau$ and linearizing, (10) becomes

$$m\ddot{z}(t) + c\dot{z}(t) + kz(t) = -wh(t)[z(t) - z(t-\tau)] \quad (11)$$

where $h(t) = \gamma(v\tau)^{\gamma-1}q(t)$ is the specific periodic cutting force variation. Equation (11) is re-written to give

$$\ddot{z}(t) + 2\xi\omega_n\dot{z}(t) + \left(\omega_n^2 + \frac{wh(t)}{m}\right)z(t) = \frac{wh(t)}{m}z(t-\tau) \quad (12)$$

that governs regenerative vibration of linear 1-DOF milling systems. The natural frequency and damping ratio of the tool system are given in terms of modal parameters k, m and c respectively as $\omega_n = \sqrt{k/m}$ and $\xi = c/2\sqrt{mk}$. These modal parameters are easily extracted from experimental plot of the tool frequency response function $R(\omega) = X/F = 1/\sqrt{(k - \omega^2 m)^2 + \omega^2 c^2}$ for forced single degree of freedom vibration.

With the substitutions $\xi_1^{(1)}(t) = z(t)$ and $\xi_2^{(1)}(t) = \dot{z}(t)$ made, (12) could be put in state differential equation form as

$$\dot{\boldsymbol{\xi}}^{(1)}(t) = \boldsymbol{A}^{(1)}\boldsymbol{\xi}^{(1)}(t) + \boldsymbol{B}^{(1)}(t)\boldsymbol{\xi}^{(1)}(t) - \boldsymbol{B}^{(1)}(t)\boldsymbol{\xi}^{(1)}(t-\tau) \quad (13)$$

where $\dot{\boldsymbol{\xi}}^{(1)}(t) = \begin{Bmatrix} \dot{\xi}_1^{(1)}(t) \\ \dot{\xi}_2^{(1)}(t) \end{Bmatrix}$, $\boldsymbol{\xi}^{(1)}(t-\tau) = \begin{Bmatrix} \xi_1^{(1)}(t-\tau) \\ \xi_2^{(1)}(t-\tau) \end{Bmatrix}$, $\boldsymbol{A}^{(1)} = \begin{bmatrix} 0 & 1 \\ -\omega_n^2 & -2\xi\omega_n \end{bmatrix}$ and $\boldsymbol{B}^{(1)}(t) = \begin{bmatrix} 0 & 0 \\ -\frac{wh(t)}{m} & 0 \end{bmatrix}$.

B. Two Degree of Freedom Model

The dynamical model shown in Fig. 5 is a 2 DOF depiction of an end-milling tool that vibrates in the $x - y$ plane (horizontal plane). The modal parameters k_x, m_x and c_x are for x−vibration while k_y, m_y and c_y are for y−vibration. The tool is symmetric when the x and y modes of vibration have identical parameters.

World Academy of Science, Engineering and Technology
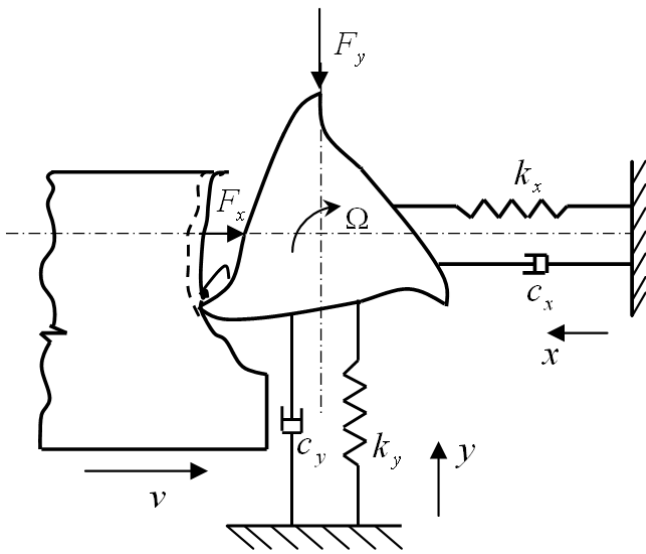International Journal of Mechanical and Mechatronics Engineering
Vol:7, No:3, 2013

Fig. 5 Dynamical model of end-milling

The governing equations of motion becomes

$$m_x\ddot{x}(t) + c_x[\dot{x}(t) - v] + k_x[x(t) - vt] + F_x(t) = 0 \quad (14a)$$

$$m_y\ddot{y}(t) + c_y\dot{y}(t) + k_yy(t) + F_y(t) = 0. \quad (14b)$$

It is seen from Fig. 4 that the x and y−components of cutting force on the tool are

$$F_x(t) = \sum_{j=1}^{N} g_j(t)[F_{\text{norm},j}(t)\sin\theta_j(t) + F_{\text{tan},j}(t)\cos\theta_j(t)] \quad (15a)$$

$$F_y(t) = \sum_{j=1}^{N} g_j(t)[-F_{\text{norm},j}(t)\cos\theta_j(t) + F_{\text{tan},j}(t)\sin\theta_j(t)]. \quad (15b)$$

The actual feed rate f_a of jth tooth at angular position $\theta_j(t)$ is inferred from Fig. 4 to be

$$f_a = [x(t) - x(t-\tau)]\sin\theta_j(t) + [y(t) - y(t-\tau)]\cos\theta_j(t) \quad (16)$$

where $x(t) = vt + x_t(t) + z_x(t)$, $y(t) = y_t(t) + z_y(t)$. The quantities $z_x(t)$ and $z_y(t)$ are respective perturbations in x and y directions. The linearized Taylor series expansion of f_a^γ about $v\tau\sin\theta_j(t)$ then reads

$$f_a^\gamma = [v\tau\sin\theta_j(t)]^\gamma + \gamma[v\tau\sin\theta_j(t)]^{\gamma-1}\{[z_x(t) - z_x(t-\tau)]\sin\theta_j(t) + [z_y(t) - z_y(t-\tau)]\cos\theta_j(t)\} \quad (17)$$

Setting $z_x(t)$ and $z_y(t)$ to zero in light of (17), (5) and (15) causes (14) to become

$$m_x\ddot{x}_t(t) + c_x\dot{x}_t(t) + k_xx_t(t) = -F_{\text{p}x}(t) \quad (18a)$$

$$m_x\ddot{y}_t(t) + c_y\dot{y}_t(t) + k_yy_t(t) = -F_{\text{p}y}(t) \quad (18b)$$

where

$$F_{px}(t) = Cw(v\tau)^\gamma \sum_{j=1}^{N} g_j(t)\sin^\gamma\theta_j(t)[\mathcal{X}\sin\theta_j(t) + \cos\theta_j(t)] \quad (19a)$$

$$F_{py}(t) = Cw(v\tau)^\gamma \sum_{j=1}^{N} g_j(t)\sin^\gamma\theta_j(t)[-\mathcal{X}\cos\theta_j(t) + \sin\theta_j(t)] \quad (19b)$$

The periodic forces $-F_{\text{p}x}(t)$ and $-F_{\text{p}y}(t)$ respectively drive the two orthogonal τ-periodic tool responses $x_t(t)$ and $y_t(t)$. Putting (18) into (14) and simplifying leads to

$$m_x\ddot{z}_x(t) + c_x\dot{z}_x(t) + k_xz_x(t) = -h_{xx}(t)[z_x(t) - z_x(t-\tau)] - h_{xy}(t)[z_y(t) - z_y(t-\tau)] \quad (20a)$$

$$m_x\ddot{z}_y(t) + c_y\dot{z}_y(t) + k_yz_y(t) = -h_{yx}(t)[z_x(t) - z_x(t-\tau)] - h_{yy}(t)[z_y(t) - z_y(t-\tau)] \quad (20b)$$

with the specific periodic cutting force variations

$$h_{xx}(t) = C\gamma(v\tau)^{\gamma-1} \sum_{j=1}^{N} g_j(t)\sin^{2\gamma}\theta_j(t)[\sin\theta_j(t) + \cos\theta_j(t)] \quad (21a)$$

$$h_{xy}(t) = C\gamma(v\tau)^{\gamma-1} \sum_{j=1}^{N} g_j(t)\sin^{2\gamma-1}\theta_j(t)\cos\theta_j(t)[\sin\theta_j(t) + \cos\theta_j(t)] \quad (21b)$$

$$h_{yx}(t) = C\gamma(v\tau)^{\gamma-1} \sum_{j=1}^{N} g_j(t)\sin^{2\gamma}\theta_j(t)[-\cos\theta_j(t) + \sin\theta_j(t)] \quad (21c)$$

$$h_{yy}(t) = C\gamma(v\tau)^{\gamma-1} \sum_{j=1}^{N} g_j(t)\sin^{2\gamma-1}\theta_j(t)\cos\theta_j(t)[-\cos\theta_j(t) + \sin\theta_j(t)] \quad (21d)$$

Equation (20) is put in matrix form to read

$$\ddot{\mathbf{z}}(t) + \mathbf{M}^{-1}\mathbf{C}\dot{\mathbf{z}}(t) + \mathbf{M}^{-1}\mathbf{K}\mathbf{z}(t) = \mathbf{M}^{-1}\mathbf{H}\mathbf{z}(t-\tau) \quad (22)$$

where $\mathbf{z}(t) = \{z_x(t) \quad z_y(t)\}^T$ and

$$\mathbf{M} = \begin{bmatrix} m_x & 0 \\ 0 & m_y \end{bmatrix}, \mathbf{C} = \begin{bmatrix} c_x & 0 \\ 0 & c_y \end{bmatrix}, \mathbf{K} = \begin{bmatrix} k_x & 0 \\ 0 & k_y \end{bmatrix},$$
$$\mathbf{H} = \begin{bmatrix} -wh_{xx}(t) & -wh_{xy}(t) \\ -wh_{yx}(t) & -wh_{yy}(t) \end{bmatrix} \quad (23)$$

Making use of state variables $\xi_1^{(2)}(t) = z_x(t)$, $\xi_2^{(2)} = \dot{z}_x(t)$, $\xi_3^{(2)}(t) = z_y(t)$ and $\xi_4^{(2)}(t) = \dot{z}_y(t)$ results in the state space form

$$\dot{\boldsymbol{\xi}}^{(2)}(t) = \mathbf{A}^{(2)}\boldsymbol{\xi}^{(2)}(t) + \mathbf{B}^{(2)}(t)\boldsymbol{\xi}^{(2)}(t) - \mathbf{B}^{(2)}(t)\boldsymbol{\xi}^{(2)}(t-\tau) \quad (24)$$

where $\boldsymbol{\xi}^{(2)}(t) = \{\xi_1^{(2)}(t) \quad \xi_2^{(2)}(t) \quad \xi_3^{(2)}(t) \quad \xi_4^{(2)}(t)\}^T$ and

$$\mathbf{A}^{(2)} = \begin{bmatrix} 0 & 1 & 0 & 0 \\ -\omega_{nx}^2 & -2\zeta\omega_{nx} & 0 & 0 \\ 0 & 0 & 0 & 1 \\ 0 & 0 & -\omega_{ny}^2 & -2\zeta\omega_{ny} \end{bmatrix}, \mathbf{B}^{(2)}(t) = \begin{bmatrix} 0 & 0 & 0 & 0 \\ -\frac{wh_{xx}(t)}{m_x} & 0 & -\frac{wh_{xy}(t)}{m_x} & 0 \\ 0 & 0 & 0 & 0 \\ -\frac{wh_{yx}(t)}{m_y} & 0 & -\frac{wh_{yy}(t)}{m_y} & 0 \end{bmatrix} \quad (25)$$

The natural frequencies and damping ratios of the tool are given in terms of modal parameters k_x, m_x, c_x, k_y, m_y and c_y respectively as $\omega_{nx} = \sqrt{k_x/m_x}$, $\omega_{ny} = \sqrt{k_y/m_y}$, $\zeta_x = c_x/2\sqrt{m_xk_x}$ and $\zeta_y = c_y/2\sqrt{m_yk_y}$.

III. CHATTER STABILITY ANALYSIS VIA MODIFIED FULL-DISCRETIZATION MAP

Equations (13) and (24) are combined in the equation

$$\dot{\boldsymbol{\xi}}^{(d)}(t) = \mathbf{A}^{(d)}\boldsymbol{\xi}^{(d)}(t) + \mathbf{B}^{(d)}(t)\boldsymbol{\xi}^{(d)}(t) - \mathbf{B}^{(d)}(t)\boldsymbol{\xi}^{(d)}(t-\tau) \quad (26)$$

World Academy of Science, Engineering and Technology
International Journal of Mechanical and Mechatronics Engineering
Vol:7, No:3, 2013

where d = 1 or 2 denotes the degree of freedom. It is written in [11] that the method of full-discretization developed by Ding et al [9] for study of milling stability starts with dividing the discrete delay τ of the system into k equal time intervals $[t_i, t_{i+1}]$ where $i = 0, 1, 2, \ldots \ldots \ldots (k-1)$ and approximating (26) as

$$\dot{\xi}^{(d)}(t) = A^{(d)}\xi^{(d)}(t) + \widetilde{\mathbf{B}}^{(d)}(t)\tilde{\xi}^{(d)}(t) - \widetilde{\mathbf{B}}^{(d)}(t)\tilde{\xi}^{(d)}(t-\tau), \ t \in [t_i, t_{i+1}] \quad (27)$$

where $t_i = i\frac{\tau}{k} = i\Delta t$,

$$\widetilde{\mathbf{B}}^{(d)}(t) = \mathbf{B}_i^{(d)} + \frac{\mathbf{B}_{i+1}^{(d)} - \mathbf{B}_i^{(d)}}{\Delta t}(t - t_i)$$
$$\tilde{\xi}^{(d)}(t) = \xi_i^{(d)} + \frac{\xi_{i+1}^{(d)} - \xi_i^{(d)}}{\Delta t}(t - t_i) \quad (28)$$
$$\tilde{\xi}^{(d)}(t-\tau) = \xi_{i-k}^{(d)} + \frac{\xi_{i+1-k}^{(d)} - \xi_{i-k}^{(d)}}{\Delta t}(t - t_i)$$

and $\xi_i^{(d)} = \xi^{(d)}(t_i)$. The basic idea of semi-discretization employed in arriving at (27) is that $\mathbf{B}^{(d)}(t)\xi^{(d)}(t)$ and $\mathbf{B}^{(d)}(t)\xi^{(d)}(t-\tau)$ are discretized while $\dot{\xi}^{(d)}(t)$ and $\xi^{(d)}(t)$ are left undiscretized. The derivation process hence follows the path to the modified full-discretization map (MFDM) that is generalized for both 1-DOF and 2-DOF end-milling processes. Definite integration of (27) in the discrete interval $[t_i, t_{i+1}]$ in light of the result $\int_{t_i}^{t_{i+1}}(t - t_i)^n dt = \Delta t^{n+1}/(n+1)$ leads to

$$\xi_{i+1}^{(d)} = e^{A^{(d)}\Delta t}\xi_i^{(d)} + \frac{\Delta t}{6}\left(\mathbf{B}_i^{(d)} + 2\mathbf{B}_{i+1}^{(d)}\right)\xi_{i+1}^{(d)} + \frac{\Delta t}{6}\left(\mathbf{B}_{i+1}^{(d)} + 2\mathbf{B}_i^{(d)}\right)\xi_i^{(d)}$$
$$- \frac{\Delta t}{6}\left(\mathbf{B}_i^{(d)} + 2\mathbf{B}_{i+1}^{(d)}\right)\xi_{i+1-k}^{(d)} - \frac{\Delta t}{6}\left(\mathbf{B}_{i+1}^{(d)} + 2\mathbf{B}_i^{(d)}\right)\xi_{i-k}^{(d)}$$
$$(29)$$

Rearranged, (29) becomes

$$\xi_{i+1}^{(d)} = \mathbf{G}^{-1}\left[e^{A^{(d)}\Delta t} + \frac{\Delta t}{6}\left(\mathbf{B}_{i+1}^{(d)} + 2\mathbf{B}_i^{(d)}\right)\right]\xi_i^{(d)} - \frac{\Delta t}{6}\mathbf{G}^{-1}\left(\mathbf{B}_i^{(d)} + 2\mathbf{B}_{i+1}^{(d)}\right)\xi_{i+1-k}^{(d)} - \frac{\Delta t}{6}\mathbf{G}^{-1}\left(\mathbf{B}_{i+1}^{(d)} + 2\mathbf{B}_i^{(d)}\right)\xi_{i-k}^{(d)}$$
$$(30)$$

where $\mathbf{G} = \mathbf{I} - \frac{\Delta t}{6}\left(\mathbf{B}_i^{(d)} + 2\mathbf{B}_{i+1}^{(d)}\right)$ and $\mathbf{I}$ is a 2d × 2d identity matrix. This is put in $2d(k + 1)$-dimensional matrix form

$$\begin{Bmatrix} \xi_{i+1}^{(d)} \\ \xi_i^{(d)} \\ \xi_{i-1}^{(d)} \\ \vdots \\ \xi_{i+1-k}^{(d)} \end{Bmatrix} = \begin{bmatrix} \mathbf{M}_{11}^i & 0 & \cdots & 0 & \mathbf{M}_{1k}^i & \mathbf{M}_{1,k+1}^i \\ \mathbf{I} & 0 & \cdots & 0 & 0 & 0 \\ 0 & \mathbf{I} & \cdots & 0 & 0 & 0 \\ \vdots & \vdots & \vdots & \vdots & \vdots & \vdots \\ 0 & 0 & 0 & 0 & \mathbf{I} & 0 \end{bmatrix} \begin{Bmatrix} \xi_i^{(d)} \\ \xi_{i-1}^{(d)} \\ \xi_{i-2}^{(d)} \\ \vdots \\ \xi_{i-k}^{(d)} \end{Bmatrix} \quad (31)$$

where $\mathbf{M}_{11}^i = \mathbf{G}^{-1}\left[e^{A^{(d)}\Delta t} + \frac{\Delta t}{6}\left(\mathbf{B}_{i+1}^{(d)} + 2\mathbf{B}_i^{(d)}\right)\right]$, $\mathbf{M}_{1k}^i = -\frac{\Delta t}{6}\mathbf{G}^{-1}\left(\mathbf{B}_i^{(d)} + 2\mathbf{B}_{i+1}^{(d)}\right)$ and $\mathbf{M}_{1,k+1}^i = -\frac{\Delta t}{6}\mathbf{G}^{-1}\left(\mathbf{B}_{i+1}^{(d)} + 2\mathbf{B}_i^{(d)}\right)$. If (31) is designated as $\mathbf{x}_{i+1} = \mathbf{M}_i\mathbf{x}_i$ then the MFDM for the system becomes

$$\mathbf{x}_k = \mathbf{M}_{k-1}\mathbf{M}_{k-2}\ldots\ldots\mathbf{M}_0\mathbf{x}_0. \quad (32)$$

The finite monodromy operator becomes

$$\mathbf{\Psi} = \mathbf{M}_{k-1}\mathbf{M}_{k-2}\ldots\ldots\mathbf{M}_0. \quad (33)$$

Equation (32) is a $2d(k + 1)$-dimensional discrete time map of the system with $\mathbf{\Psi}$ acting as a linear operator that transforms the delayed state $\mathbf{x}_0$ to the present state $\mathbf{x}_k$.

Suppose by a suitable model transformation method, (26) is completely transformed into an infinite dimensional periodic ordinary differential equation $\dot{w}(t) = \mathbf{C}(t)w(t)$ with solution $w(t) = \mathbf{\Psi}(t)w(0)$. The extended Floquet theory gives that the state transition matrix $\mathbf{\Psi}(t)$ is given by $\mathbf{\Psi}(t) = \mathbf{P}(t)e^{\mathbf{B}t}$ where $\mathbf{B}$ is a constant infinite square matrix, $\mathbf{P}(t)$ is τ-periodic and has initial condition of identity matrix. Use made of similarity transformation of second rank tensors results in the solution $w(t)$ having the form $w(t) = \mathbf{P}(t)\mathbf{V}e^{\mathbf{D}t}\mathbf{V}^{-1}w(0)$ where $\mathbf{V}$ is the matrix of eigen-vectors of $\mathbf{B}$ and $\mathbf{D}$ is a diagonal matrix with eigen-values of $\mathbf{B}$ as non-zero elements. The condition for asymptotic stability of $w(t)$ thus becomes that each of the infinitely many eigen-values of $\mathbf{B}$ has a negative real part. The monodromy matrix now becomes $\mathbf{\Psi}(\tau) = \mathbf{V}e^{\mathbf{D}\tau}\mathbf{V}^{-1}$. Since the eigenvectors of monodromy matrix $\mathbf{\Psi}(\tau)$ are identical with those of $\mathbf{B}$, similarity transformation results in

$$\mathbf{M} = e^{\mathbf{D}\tau} \quad (34)$$

where $\mathbf{M}$ is a diagonal matrix with eigen-values of $\mathbf{\Psi}(\tau)$ as elements. It can be seen from (34) that the relationship between eigen-values of $\mathbf{\Psi}(\tau)$ designated μ_i and eigen-values of $\mathbf{B}$ designated λ_i is

$$\mu_i = e^{\lambda_i \tau} \quad (35)$$

If $\lambda_i = \sigma + j\omega$ then $|\mu_i| = e^{\sigma\tau}$. This means that the necessary and sufficient condition for asymptotic stability of the system is that each of the eigenvalues of $\mathbf{\Psi}(\tau)$ has a magnitude that is less than one. In other words, all the eigen-values of the matrix $\mathbf{\Psi}(\tau)$ must exist within a unit circle centred at the origin of the complex plane. If the eigenvalue of $\mathbf{\Psi}(\tau)$ with highest magnitude is designated $\mu_{\max}$ the stability transition curve of (26) is tracked by locating the critical parameter combinations that allow $|\mu_{\max}| = 1$. Most the eigenvalues of $\mathbf{\Psi}(\tau)$ are clustered around the origin of the unit circle [12] enabling the finite monodromy operator $\mathbf{\psi}$ (given by (33)) to capture $\mu_{\max}$ when approximation parameter k is big enough. Realistic condition for asymptotic stability of the system now becomes that each of the $2d(k + 1)$ eigenvalues of $\mathbf{\psi}$ has a magnitude that is less than one.

IV. RESULTS, VALIDATION AND DISCUSSIONS

Stability charts are generated for both 1-DOF and symmetric 2-DOF chatter of full-immersion end-milling processes with parameters; $m = 0.431\text{kg}, \omega_n = 5700 \text{ rads}^{-1}, \xi = 0.02, C = 3.5 \times 10^7 \text{Nm}^{-7/4}, v = 0.0025 \text{ms}^{-1}$ and $\mathcal{X} = 0.3$. These are shown

World Academy of Science, Engineering and Technology
International Journal of Mechanical and Mechatronics Engineering
Vol:7, No:3, 2013

in Fig. 6 for one tooth end-miller, Fig. 7 for two tooth end-miller, Fig. 8 for three tooth end-miller, Fig. 9 for six tooth end-miller, Fig. 10 for eight tooth end-miller, and Fig. 11 for ten tooth end-miller. Eigen-values of $\boldsymbol{\psi}$ are calculated for the low-speed charts with $k = 50$ on a 200 by 25 data grid with spindle speed steps $\Delta\Omega = 50$rpm and depth of cut steps $\Delta w = 0.0003$m. The high speed charts utilized $k = 35$ on a 200 by 25 data grid with $\Delta\Omega = 210.5$rpm and $\Delta w = 0.0003$m. The stability transition curves connect points that satisfy condition $|\mu_{max}| = 1$. The sub-domain of asymptotic stability is grey in each of the stability charts while that of instability is dark. Stability chart for 1-DOF chatter is placed adjacent to that of 2-DOF chatter of each miller for direct comparison. Both low speed range 100rpm $\leq \Omega \leq$ 10100rpm and high-speed range 8000rpm $\leq \Omega \leq$ 50100rpm are considered for each miller. 2-DOF analysis seems to give a much more conservative result since its stable domain is always much smaller than that of 1-DOF analysis. This observation is clearer from looking at the vertical scales of any two adjacent charts. Flip bifurcation lobes are seen for one, two and three tooth fully-immersed 1-DOF end-milling but not for the corresponding 2-DOF cases.

The validity of these charts is based on MATLAB dde23 solution of (26) at selected points of the parameter space. Stable MATLAB dde23 solutions for the fully-immersed three tooth end-miller exhibit converging orbits at points marked with star while the unstable (chatter) solutions exhibit diverging orbits at points marked with diamond in Fig. 8. It is thus seen that a very good agreement exists between MATLAB dde23 analysis and the generated charts. MATLAB dde23 solutions of two sample points of 1-DOF chatter of three tooth miller are presented in Fig. 12 while those of 2-DOF system are presented in Fig. 13. MATLAB dde23 solutions of each of the sample points is generated as both a trajectory and an orbit and placed side by side. Each of the trajectories clearly reflects stability or instability of perturbation velocity but with erroneous impression that perturbation displacement is coincident with time axis. Each of the orbits complements judgment by correcting this visual error. Since no consideration is given to perturbation history in the discrete mapping that led to $\boldsymbol{\psi}$, any choice of history (even stochastic perturbation history of real milling processes) is not expected to affect stability. This explains why MATLAB dde23 solutions of (26) that are based on the arbitrarily chosen constant perturbation history $\{\xi_1^1(t) \quad \xi_2^1(t)\}^T = \{10^{-7}m \quad 10^{-6}ms^{-1}\}^T$, $t\epsilon[-\tau, 0]$ agree with the stability charts of 1-DOF three tooth end-miller while solutions based on the history $\{\xi_1^2(t) \quad \xi_2^2(t) \quad \xi_3^2(t) \quad \xi_4^2(t)\}^T = \{10^{-7}m \quad 10^{-6}ms^{-1} \quad 10^{-7}m \quad 10^{-6}ms^{-1}\}^T$, $t\epsilon[-\tau, 0]$ agree with stability charts of 2-DOF three tooth end-miller.
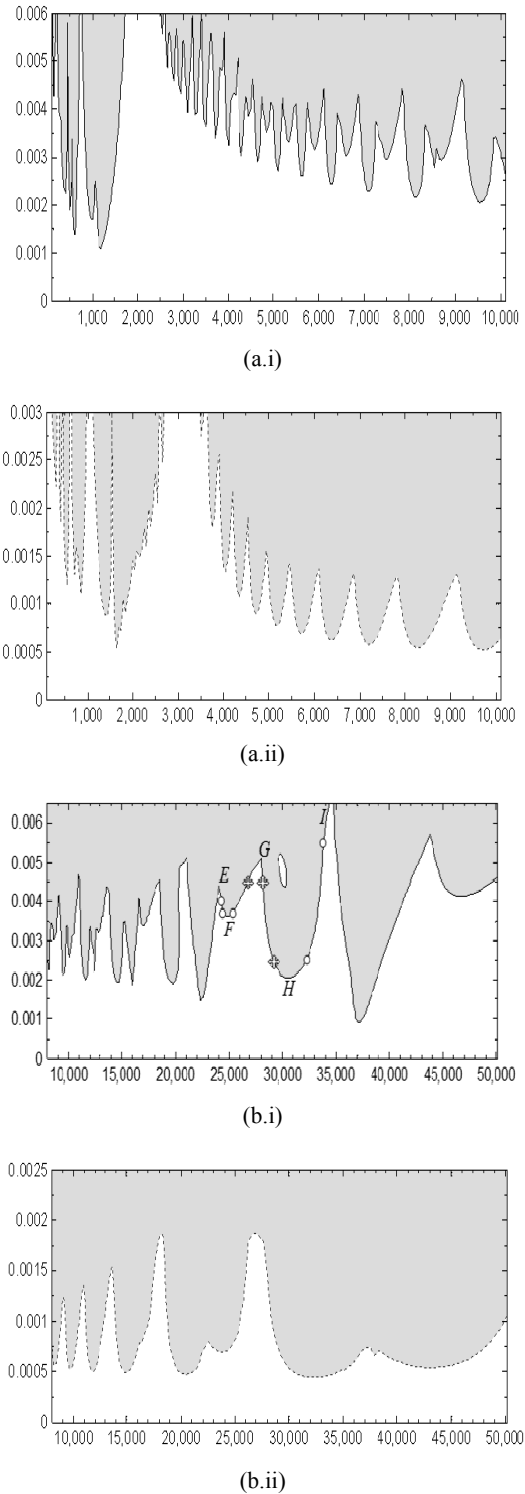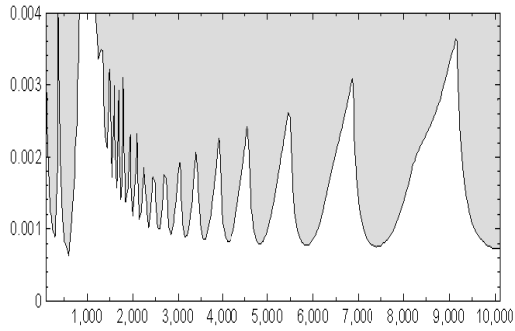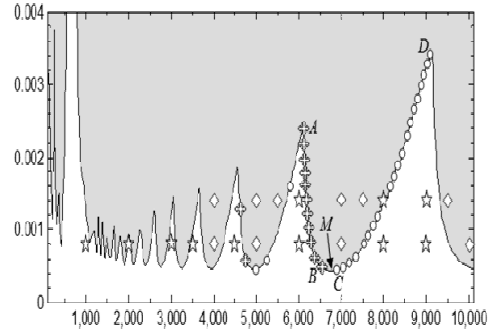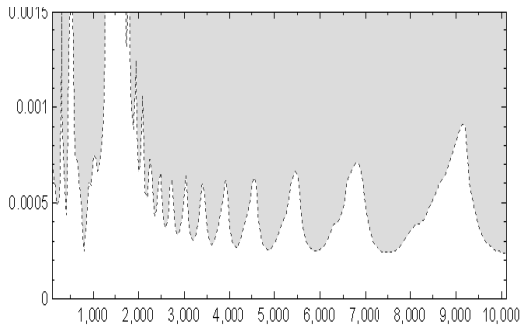

(a.i)

(a.ii)

(b.i)

(b.ii)

Fig. 6 Stability charts of full-immersion one tooth end-milling, grey and dark subdomains are for stable and chatter operations respectively. (a.i) Low speed chart of 1-DOF end-milling (a.ii) Low speed chart of 2-DOF end-milling (b.i) High speed chart of 1-DOF end-milling (b.ii) High speed chart of 2-DOF end-milling
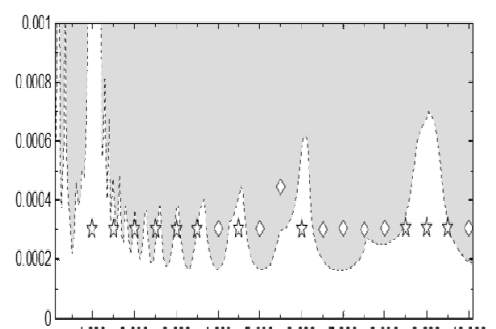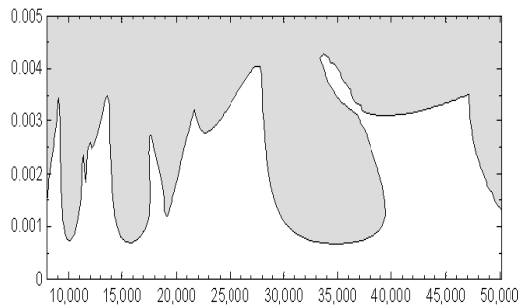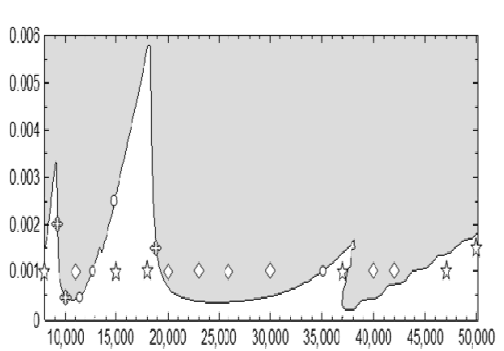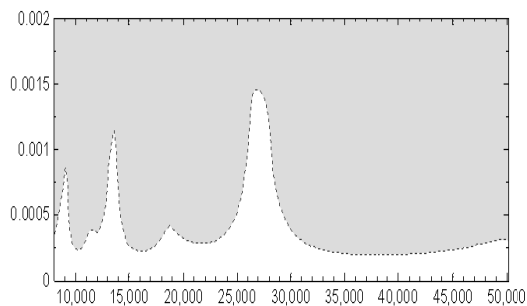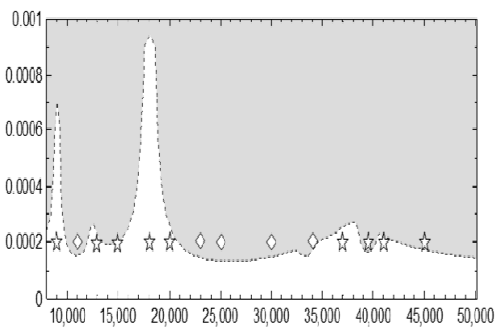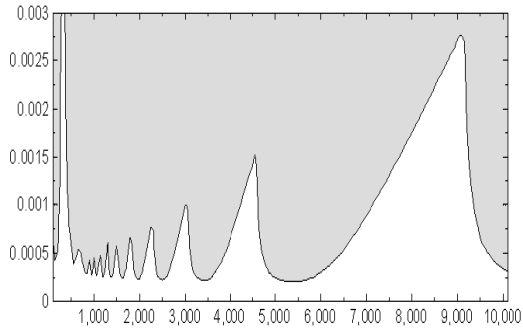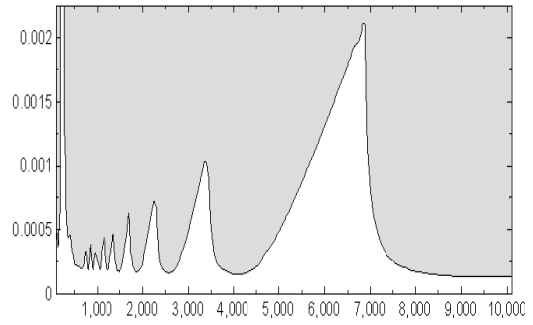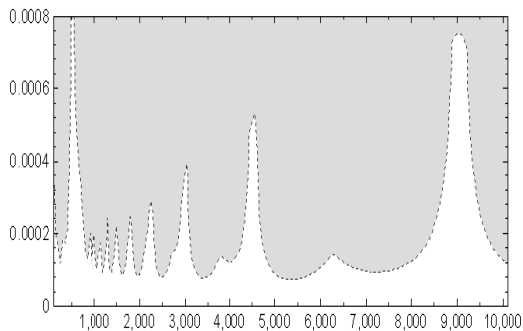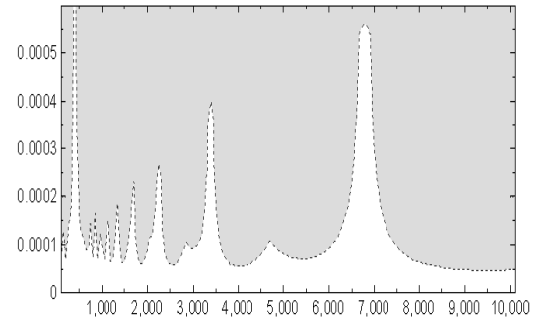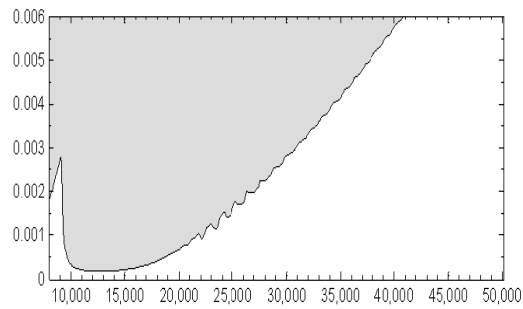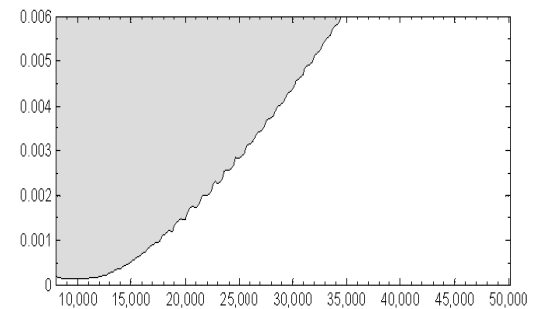
World Academy of Science, Engineering and Technology
International Journal of Mechanical and Mechatronics Engineering
Vol:7, No:3, 2013

(a.i)

(a.ii)

(b.i)

(b.ii)

Fig. 7 Stability charts of full-immersion two tooth end-milling, grey and dark subdomains are for stable and chatter operations respectively. (a.i) Low speed chart of 1-DOF end-milling (a.ii) Low speed chart of 2-DOF end-milling (b.i) High speed chart of 1-DOF end-milling (b.ii) High speed chart of 2-DOF end-milling
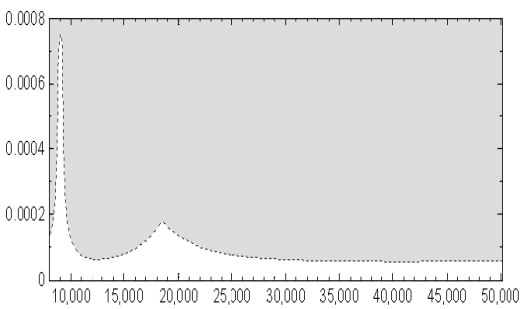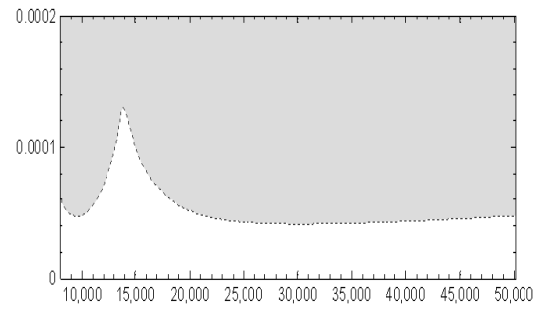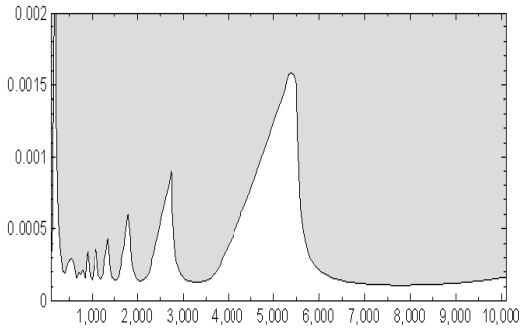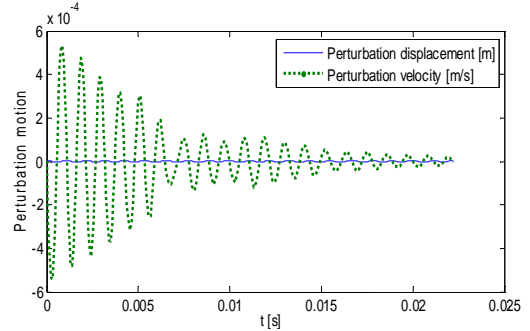

(a.i)

(a.ii)

(b.i)

(b.ii)

Fig. 8 Stability charts of full-immersion three tooth end-milling, grey and dark subdomains are for stable and chatter operations respectively. Star and diamond are marks for stable and unstable MATLAB dde23 solutions respectively. (a.i) Low speed chart of 1-DOF end-milling (a.ii) Low speed chart of 2-DOF end-milling (b.i) High speed chart of 1-DOF end-milling (b.ii) High speed chart of 2-DOF end-milling

World Academy of Science, Engineering and Technology
International Journal of Mechanical and Mechatronics Engineering
Vol:7, No:3, 2013

(a.i)

(a.ii)

(b.i)

(b.ii)

Fig. 9 Stability charts of full-immersion six tooth end-milling, grey and dark subdomains are for stable and chatter operations respectively. (a.i) Low speed chart of 1-DOF end-milling (a.ii) Low speed chart of 2-DOF end-milling (b.i) High speed chart of 1-DOF end-milling (b.ii) High speed chart of 2-DOF end-milling
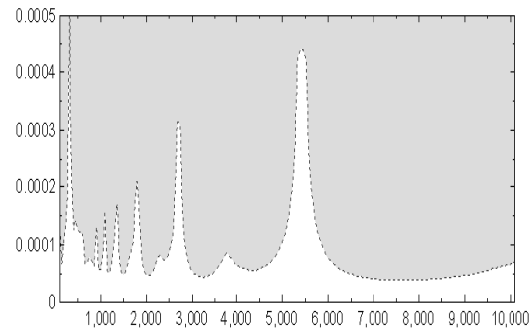
(a.i)

(a.ii)

(b.i)

(b.ii)

Fig. 10 Stability charts of full-immersion eight tooth end-milling, grey and dark subdomains are for stable and chatter operations respectively. (a.i) Low speed chart of 1-DOF end-milling (a.ii) Low speed chart of 2-DOF end-milling (b.i) High speed chart of 1-DOF end-milling (b.ii) High speed chart of 2-DOF end-milling
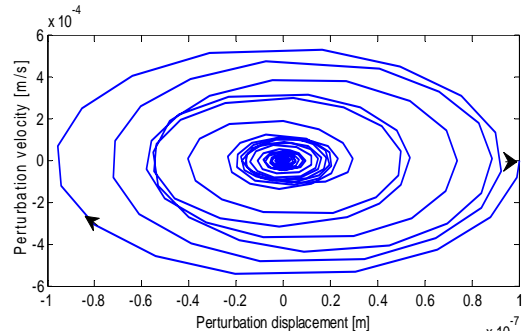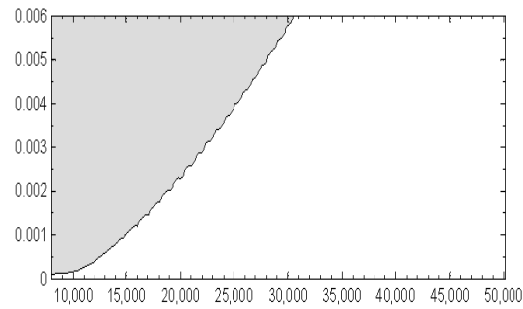
World Academy of Science, Engineering and Technology
International Journal of Mechanical and Mechatronics Engineering
Vol:7, No:3, 2013

(a.i)

(a.ii)

(b.i)

(b.ii)

Fig. 11 Stability charts of full-immersion ten tooth end-milling, grey and dark subdomains are for stable and chatter operations respectively. (a.i) Low speed chart of 1-DOF end-milling (a.ii) Low speed chart of 2-DOF end-milling (b.i) High speed chart of 1-DOF end-milling (b.ii) High speed chart of 2-DOF end-milling
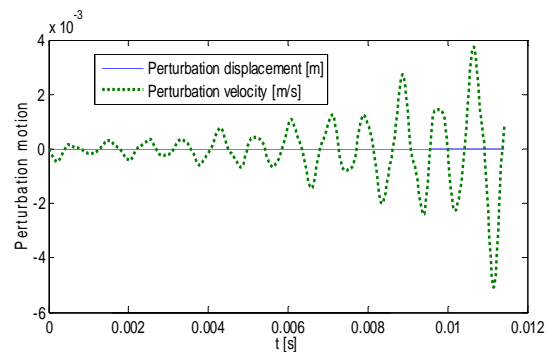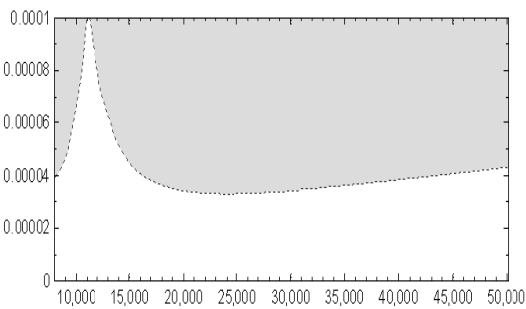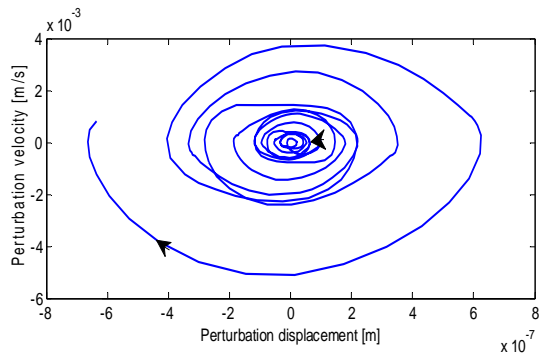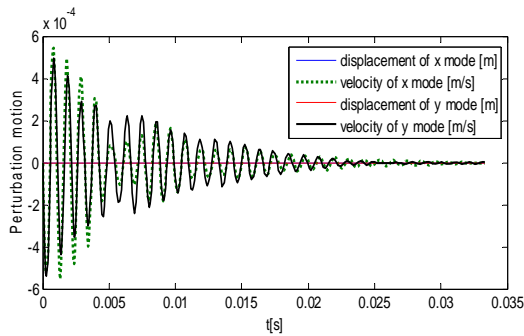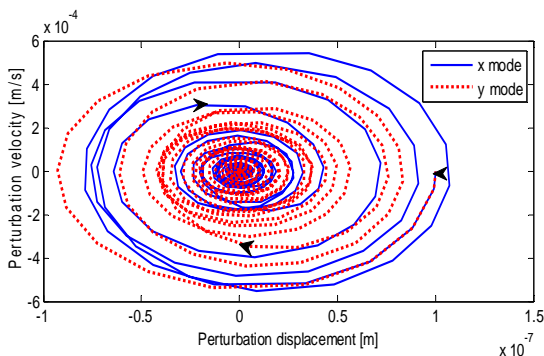

(a.i)

(a.ii)

(b.i)

(b.ii)

Fig. 12 MATLAB dde23 solutions of fully-immersed 1-DOF three tooth end-miller with history
$\{\xi_1^1(t) \quad \xi_2^1(t)\}^T = \{10^{-7}\text{m} \quad 10^{-6}\text{ms}^{-1}\}^T$, $t\epsilon[-\tau, 0]$ is (a) stable at $(\Omega, w) = (4500\text{rpm}, 0.0008\text{m})$ (a.i) solution as a trajectory (a.ii) solution as an orbit. (b) unstable at $(\Omega, w) = (35000\text{rpm}, 0.003\text{m})$ $\Omega = 35000\text{rpm}$ (b.i) solution as a trajectory (b.ii) solution as an orbit

World Academy of Science, Engineering and Technology
International Journal of Mechanical and Mechatronics Engineering
Vol:7, No:3, 2013

(a.i)

(a.ii)
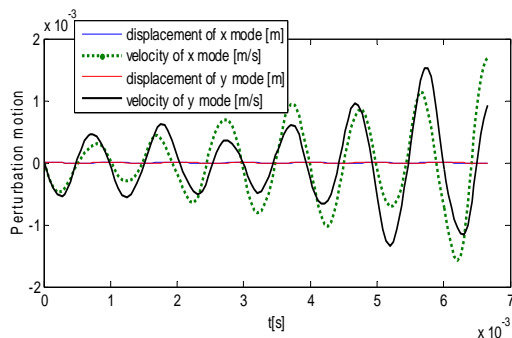
(b.i)

(b.ii)
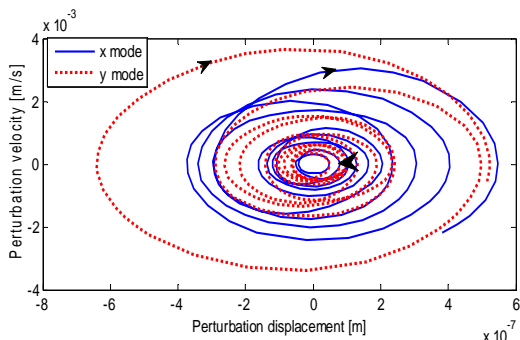
Fig. 13 MATLAB dde23 solutions of fully-immersed 2-DOF three tooth end-miller with history $\{\xi_1^2(t) \quad \xi_2^2(t) \quad \xi_3^2(t) \quad \xi_4^2(t)\}^T = \{10^{-7}\mathrm{m} \quad 10^{-6}\mathrm{ms}^{-1} \quad 10^{-7}\mathrm{m} \quad 10^{-6}\mathrm{ms}^{-1}\}^T$, $t\epsilon[-\tau, 0]$ is (a) stable at (Ω, w)= (6000rpm, 0.0004m) (a.i) solution as a trajectories (a.ii) solution as an orbits (b) unstable at (Ω, w)= (30000rpm, 0.0005m) (b.i) solution as a trajectories (b.ii) solution as an orbits

Some selected critical parameter combinations are inserted into the monodromy matrix of 1-DOF full-immersion end-milling and the critical characteristic multipliers μ_c extracted. All the secondary Hopf bifurcation lobes (SHBL's) of full-immersion end-milling with simultaneous teeth engagement (end-millers with number of teeth $N \geq 3$) exhibit a simple but unique behaviour. Each of such SHBL's has a single minimum point (point M of the SHBL labeled ABCD in Fig. 8 (a.i) for example) at which μ_c are almost pure imaginary. The lower spindle speed portion (LSSP) of each such SHBL is the portion at the left of the minimum point while the higher spindle speed portion (HSSP) is the portion at the right of the minimum point. It is seen that secondary Hopf bifurcation occurs in the right-half plane of the unit circle centred at the origin of the complex plane at any point in the LSSP (Fig. 14 (a)). Secondary Hopf bifurcation occurs in the left-half plane of the unit circle at any point in the HSSP (Fig. 14 (b)). The positive real part of μ_c decreases in size from about unity to about zero as critical parameter combination moves from start of the LSSP towards the minimum point. The negative real part of μ_c increases in magnitude from about zero to about unity as critical parameter combination moves away from the minimum point along the HSSP. The SHBL marked ABCD on the stability chart of low-speed three tooth end-miller (Fig. 8 (a.i)) has the LSSP portion studded with crosses with the positive Re(μ_c) monotonically decreasing from A to B. The portion studded with circles is the HSSP that exhibits negative Re(μ_c) that monotonically increases in magnitude from C to D.
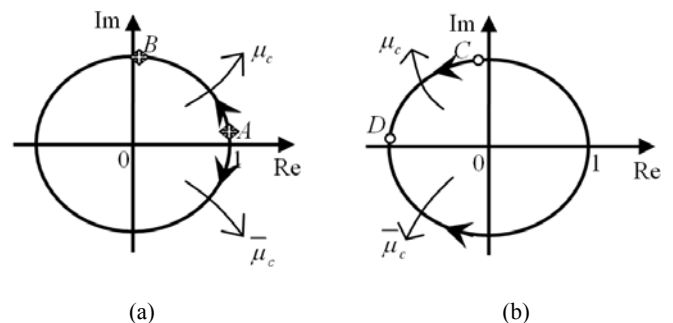

(a)   (b)

Fig. 14 For $N \geq 3$ (a) secondary Hopf bifurcation occurs in the right-half portion of the unit circle at any point in the LSSP of each SHBL (b) secondary Hopf bifurcation occurs in the left-half portion of the unit circle at any point in the HSSP of each SHBL.

From (36) results that bifurcations occur according to the equation

$$\mu_c = e^{\mathrm{j}\omega_c\tau} = \cos\omega_c\tau + \mathrm{j}\sin\omega_c\tau \qquad (37)$$

The quantity $\omega_c\tau$ can be considered as an angle that varies as critical parameter combination changes from the start to the end of a SHBL. For example the variation of $\omega_c\tau$ as critical parameter combination moves from A to D along the marked SHBL of three tooth miller shown in Fig. 8 (a.i) is as follows; $\omega_c\tau = 2\pi n \pm \epsilon$ at the inception of the lobe (point A) with

World Academy of Science, Engineering and Technology
International Journal of Mechanical and Mechatronics Engineering
Vol:7, No:3, 2013

$\epsilon > 0$ and $n = 0, 1, 2, ...$ The small positive quantity ϵ is introduced to uphold the condition that period one bifurcation does not occur in milling process. It then varies to $\omega_c\tau = 2\pi(n \pm 1/4)$ in the neighbourhood of the minimum point M. Variation finally occurs from $\omega_c\tau = 2\pi(n \pm 1/4)$ close to M to about $\omega_c\tau = 2\pi(n \pm 1/2)$ at the end of the lobe (point D) where flip bifurcation is expected to occur. Same trend in $\omega_c\tau$ occurs in the next SHBL. This trend means that a flip bifurcation lobe (FBL) is expected to connect two adjacent SHBL's. Invisibility of a connecting FBL may not necessarily mean that it is non-existent but could mean that it is too small in size to be seen. Since $\omega_c = \omega_c(\tau, w)$ the quantity $\omega_c\tau$ is also a function of τ and w. Stability charts are normally generated on a data grid of constant mesh size. Suppose the distance between two adjacent mesh points in Ω direction is $\Delta\Omega$ then the fractional change incurred in τ due to fractional change in spindle speed $f_\Omega = \Delta\Omega/\Omega$ is $f_\tau = \Delta\tau/\tau = (1 + f_\Omega)^{-1} - 1$. In the limit when $\Omega \to \infty$, the ratio $f_\tau \to 0$. If for the three tooth miller, variation in $\omega_c\tau$ derives predominantly from variation in τ then more $\Delta\Omega$'s will be needed to cause $\omega_c\tau$ traverse about π radians need for generation of a SHBL. This could be part of the reasons why bifurcation lobes get bigger and more visible as Ω rises. A FBL could be too small to be seen when Ω is too small such that single $\Delta\Omega$ change in Ω could cause too much change in $\omega_c\tau$ that the condition for flip bifurcation $\omega_c\tau = 2\pi n \pm \pi$ (which is a very restrictive condition when compared with the restriction for secondary Hopf Bifurcation $0 < |\omega_c\tau| < |2\pi n \pm \pi|$) is not allowed to be met. If Ω is high enough the condition for flip bifurcation could approximately be met in the event of multiple $\Delta\Omega$ change in Ω. These could be part of the reasons why FBL is invisible in the low speed chart but visible in the high speed chart of the fully-immersed three-tooth miller (see Figs. 8 (a.i) and (b.i)).

One special thing the about fully-immersed three-tooth miller is that it acts as a boundary case because when $N < 3$ some SHBL's exhibit more than one turning point. An example of such a curve is marked EFGHI in the high-speed stability chart of fully immersed one tooth miller (Fig. 6 (b.i)). Sample points are marked with cross or circle depending on whether $Re(\mu_c)$ is positive or negative. Increasing in N of full-immersion end-milling causes decrease in the range of specific cutting force variation $h(t) = \gamma(v\tau)^{\gamma-1}q(t)$. The implication is that periodic DDE governing end-milling processes approaches autonomous DDE governing the turning processes as N increases (milling with infinite number of cutting edges is dynamically equivalent with the turning process). Thus flip Bifurcation, which does not have any meaning in turning process is expected to disappear in full-immersion end-milling when N gets higher. This could be the reason why flip bifurcation lobes are not seen in the stability charts of six, eight and ten tooth 1-DOF end-miller as seen in Figs. 9 (a.i), (b.i); 10 (a.i), (b.i); 11 (a.i), and (b.i).

V. CONCLUSION

Stability analysis of a full-immersion end-milling with the parameters; tool mass $m = 0.0431$kg, tool natural frequency $\omega_n = 5700$ rads^{-1}, damping factor $\xi = 0.02$ and workpiece cutting coefficient $C = 3.5 \times 10^7$Nm$^{-7/4}$ results in transition curves that demarcate parameter planes of spindle speed and depth of cut into stable and unstable sub-domains . A modified map of full-discretization method that is generalized for both 1-DOF and 2-DOF end-milling is utilized. Both 1-DOF and 2-DOF cases are considered for each of one, two, three, six, eight and ten tooth end-millers. Stability chart of each 2-DOF case is generally seen to be much more conservative (has much smaller stable sub-space) than the corresponding 1-DOF case. The validity of the charts is based on agreement with MATLAB dde23 analysis of governing periodic DDE at selected points of the parameter space. It is noted that the agreement between the stability charts and MATLAB dde23 solutions is not affected by the choice of initial history of governing periodic DDE.

It is found that when the number of teeth $N \geq 3$, fully immersed 1-DOF end-milling has secondary Hopf bifurcation lobes (SHBL's) that exhibit one minimum point each. At each minimum point, critical characteristic multipliers are almost pure imaginary. Each of such SHBL has two distinguished parts, namely; the Lower Spindle Speed Portion (LSSP) placed left of the minimum point and Higher Spindle Speed Portion (HSSP) placed right of the minimum point. Secondary Hopf bifurcation occurs only in the right-half side of the unit circle in the LSSP and occurs only in the left-half side of the unit circle in HSSP. It is found that bifurcation lobes generally get bigger and more visible with increase in spindle speed because bigger spindle speed range is need for generation of a complete SHBL as spindle speed increases. It is discovered that the real part of critical characteristic multipliers varies from about 1 to about 0 as a critical point moves from start of LSSP towards the minimum point. When the critical point moves along HSSP away from the minimum point the real part of critical characteristic multipliers varies from about 0 to about -1. This means that bifurcation gets towards flip towards the end of a SHBL. It is concluded in this work that even when flip bifurcation is not seen, it is expected to occur in the immediate vicinity of intersection of two SHBL's.

REFERENCES

[1] G. Stépán, R. Szalai, and T. Insperger, "Nonlinear Dynamics of High-Speed Milling Subjected to Regenerative Effect," in *Nonlinear Dynamics of Production Systems,* Gunther Radons, Ed. New York: Wiley-VCH, 2003, pp.1-2.

[2] M.A. Davies, T. J. Burns and T. L. Schmitz, "High-Speed Machining Processes: Dynamics of Multiple Scales*," National Institute of Standards and Technology,* 100 Bureau Drive, Gaithersburg MD 20899, USA, 1999.

[3] T. Insperger, B.P. Mann, G. Stepan, and P.V. Bayly, *"*Stability of up-milling and down-milling, part 1: alternative analytical methods," *International Journal of Machine Tools and Manufacture* vol. 43, 2003, pp. 25–34.

[4] O. A. Bobrenkov , F. A. Khasawneh , E. A. Butcher, and B. P. Mann, "Analysis of milling dynamics for simultaneously engaged cutting teeth," *Journal of Sound and Vibration,* vol 329, 2010, pp. 585–606.

World Academy of Science, Engineering and Technology
International Journal of Mechanical and Mechatronics Engineering
Vol:7, No:3, 2013

[5] E. A. Butcher, H. Ma, E. Bueler, V. Averina, and Z. Szabo, "Stability of linear time-periodic delay-differential equations via Chebyshev polynomials," *International Journal for Numerical Methods in Engineering,* vol. 59, 2004 pp. 895–922.

[6] T. Insperger*,* and G. Stepan, "Semi-discretization method for delayed systems*," International Journal For Numerical Methods In Engineering*, vol. 55, 2002, pp. 503–518.

[7] T. Insperger, and G. Stepan, "Stability of Milling Process*," Periodica Polytechnica,* vol. 44, no 1, 2000, pp. 47–57.

[8] C. G. Ozoegwu, "Chatter of Plastic Milling CNC Machine: Master of Engineering thesis*," Nnamdi Azikiwe University Awka, 2011.*

[9] Y. Ding, L.M. Zhu, X.J. Zhang and H. Ding, "A full-discretization method for prediction of milling stability," *International Journal of Machine Tools and Manufacture* vol. 50, 2010, pp. 502–509.

[10] T. Insperger, "Stability Analysis of Periodic Delay-Differential Equations Modelling Machine Tool Chatter*:* PhD dissertation*," Budapest University of Technology and Economics, 2002.*

[11] T. Insperger, "Full-discretization and semi-discretization for milling stability prediction: Some comments*," International Journal of Machine Tools and Manufacture* vol. 50, 2010, pp. 658–662.

[12] E. Butcher, and B. P. Mann, "Stability Analysis and Control of Linear Periodic Delayed Systems using Chebyshev and Temporal Finite Element Methods," *http://mae.nmsu.edu/faculty/eab/ bookchapter_final.pdf.*